

# **Design of Metal-Organic Molecular Precursors for Atomic Layer Deposition**

Jan Gerkens

OPTIMEDIEN





Georg-August-Universität Göttingen

Design of Metal-Organic Molecular Precursors  
for Atomic Layer Deposition

Dissertation zur Erlangung des mathematisch-naturwissenschaftlichen  
Doktorgrades

„DOCTOR RERUM NATURALIUM“  
der Georg-August-Universität Göttingen

im Promotionsprogramm der  
Georg-August University School of Science (GAUSS)

vorgelegt von  
Jan Gerkens  
aus Buxtehude

Göttingen 2019

### **Bibliografische Information der Deutschen Bibliothek**

Die Deutsche Bibliothek verzeichnet diese Publikation in der Deutschen Nationalbibliografie; detaillierte bibliografische Daten sind im Internet über <http://dnb.ddb.de> abrufbar.

### **Jan Gerkens**

Design of Metal-Organic Molecular Precursors for Atomic Layer Deposition  
ISBN 978-3-86376-182-0

### **Betreuungsausschuss**

Prof. Dr. Sven Schneider  
Institut für Anorganische Chemie, Georg-August-Universität Göttingen  
Prof. Dr. Franc Meyer  
Institut für Anorganische Chemie, Georg-August-Universität Göttingen

### **Mitglieder der Prüfungskommission**

Referent: Prof. Dr. Sven Schneider  
Institut für Anorganische Chemie, Georg-August-Universität Göttingen  
Korreferent: Prof. Dr. Franc Meyer  
Institut für Anorganische Chemie, Georg-August-Universität Göttingen

### **Weitere Mitglieder der Prüfungskommission**

Prof. Dr. Manuel Alcarazo  
Institut für Organische und Biomolekulare Chemie, Georg-August-Universität Göttingen  
Dr. Oliver Bünermann  
Institut für Physikalische Chemie, Georg-August-Universität Göttingen  
Jun.-Prof. Dr. Nathalie Kunkel  
Institut für Anorganische Chemie, Georg-August-Universität Göttingen  
Dr. Christian Sindlinger  
Institut für Anorganische Chemie, Georg-August-Universität Göttingen

**Tag der mündlichen Prüfung: 11.12.2019**

### **Alle Rechte vorbehalten**

1. Auflage 2020

© Optimedien Verlag e.K., Göttingen

URL: [www.optimedien.com](http://www.optimedien.com)

Printed in Germany

Papier ist FSC zertifiziert (holzfrei, chlorfrei und säurefrei, sowie alterungsbeständig nach ANSI 3948 und ISO 9706). Das Werk, einschließlich aller seiner Teile, ist urheberrechtlich geschützt. Jede Verwertung außerhalb der engen Grenzen des Urheberrechtsgesetzes in Deutschland ist ohne Zustimmung des Verlages unzulässig und strafbar. Dies gilt insbesondere für Vervielfältigungen, Übersetzungen, Mikroverfilmungen und die Einspeicherung und Verarbeitung in elektronischen Systemen.

# Danksagung

Für die Motivation, Geduld, Freiheit und die Anleitung während meiner Promotion möchte ich meinem Betreuer PROF. DR. SVEN SCHNEIDER von ganzem Herzen danken. PROF. DR. FRANC MEYER danke ich für die Übernahme des Koreferats. Den übrigen Mitgliedern der Prüfungskommission sei ebenfalls gedankt.

DR. CHRISTIAN WÜRTELE und DR. MARKUS FINGER danke ich für die allgemeine Unterstützung während meiner Zeit in der Gruppe, sowie für die Bereitstellung Ihrer Expertise in den Gebieten der Röntgenstrukturanalyse bzw. der theoretischen Chemie. DALILA GRIFFIN und DR. CLAUDIA STÜCKL danke ich für die kompetente Unterstützung in allen administrativen Fragen. DR. SERHIY DEMESHKO danke ich für die Durchführung und Auswertung der SQUID-Experimente. Mein Dank geht auch an DMITRY ALDAKOV und ROBERT KÖHLER für die Durchführung der XPS Experimente.

Für interessante Einblicke in die Welt der Industrieforschung während einer Forschungs- und Entwicklungskollaboration danke ich DR. TORBEN ADERMANN und DR. HAGEN WILMER von der BASF.

Die letzten fünf Jahre werden mit Sicherheit zu den besten meines Lebens zählen. Besonders dazu beigetragen hat der gesamte Arbeitskreis Schneider, welcher mir durch seine offene Arbeitsatmosphäre schnell wie ein zweites zu Hause war. Besonderer Dank geht dabei an DR. MARKUS SCHEIBEL, DR. CHRISTIAN VOLKMANN und DR. JOSH ABBENSETH, die mir sowohl fachlich als auch menschlich eine reibungslose Aufnahme in die Gruppe ermöglicht haben. Weiterhin möchte ich meinen langjährigen LaborkollegInnen (mittlerweile Freunden) DR. FLORIAN WÄTJEN, BASTIAN SCHLUSCHASS, DR. FELIX SCHNECK und RICHT VAN ALTEN für die unvergessliche Zeit danken. Besonderer Dank für das Korrekturlesen dieser Arbeit geht an DR. JOSH ABBENSETH, DR. FELIX SCHNECK und RICHT VAN ALTEN. Danken möchte ich außerdem FENGXIA LI, die mit Ihrer Wissbegierde und Ihrem Fleiß eine große Unterstützung war.

Zu guter Letzt möchte ich meiner Familie danken, welche durch Ihre Unterstützung in allen Belangen mein Studium erst ermöglicht haben.



# Table of Contents

List of Figures.....	IV
List of Schemes.....	XII
List of Tables.....	XIII
Abbreviations.....	XV
<b>1 Introduction.....</b>	<b>1</b>
1.1 The Versatile Chemistry of Low-coordinate Transition Metal Amides .....	1
1.2 Molecular Magnetism of Low-Valent Transition Metal Compounds .....	4
1.2.1 Origins of Molecular Magnetism.....	4
1.2.2 3d Metal Amides as Single Ion Molecular Magnets....	7
1.3 Atomic Layer Deposition .....	9
1.3.1 Deposition of Thin Films .....	9
1.3.2 Concepts and Requirements.....	12
1.3.3 Precursors for Atomic Layer Deposition .....	18
1.4 ALD and Metal Amides in Application.....	21
1.4.1 Challenges in Miniaturization.....	21
1.4.2 Challenges in Future Energy Supply .....	23
1.5 Scope of this work .....	26
<b>2 Results &amp; Discussion.....</b>	<b>29</b>
2.1 Low-coordinate Cobalt Silylamido Complexes.....	29
2.1.1 The Gas Phase: Cobalt Silylamido Complexes as Precursors for Atomic Layer Deposition. ....	29

2.1.2	The Solid State: Molecular Magnetism .....	36
2.1.3	The Liquid Phase: Properties and Dissociation Equilibria in Solution.....	45
2.2	Properties and Reactivity of Nickel Silylamido complexes .....	57
2.3	Deposition Experiments.....	64
2.3.1	Atomic Layer Deposition of TaS <sub>2</sub> .....	65
2.3.2	Atomic Layer Deposition and Electrochemical Properties of MoS <sub>2</sub> .....	68
<b>3</b>	<b>Conclusion and Outlook.....</b>	<b>75</b>
<b>4</b>	<b>Experimental Section.....</b>	<b>77</b>
4.1	Methods .....	77
4.1.1	General Remarks.....	77
4.1.2	Atomic Force Microscopy (AFM).....	77
4.1.3	Elemental Analysis .....	77
4.1.4	NMR-Spectroscopy .....	77
4.1.5	Profilometry .....	78
4.1.6	Scanning Electron Microscopy (SEM).....	78
4.1.7	SQUID .....	78
4.1.8	Temperature Stabilization Tests.....	78
4.1.9	Thermogravimetric Analysis (TGA).....	78
4.1.10	UV-Vis-Spectroscopy.....	79
4.1.11	X-Ray Diffraction .....	79
4.1.12	X-ray Photoelectron Spectroscopy (XPS) .....	79
4.2	Synthesis and Characterization.....	80

---

4.2.1	[Co(N(SiMe <sub>3</sub> ) <sub>2</sub> ) <sub>2</sub> ] (1) .....	80
4.2.2	[Co(N(SiMe <sub>3</sub> ) <sub>2</sub> )(THF)] (2).....	80
4.2.3	[Co(N(SiMe <sub>3</sub> ) <sub>2</sub> )(PR <sub>3</sub> )] (3 a-d) .....	81
4.2.4	[Co(N(SiMe <sub>3</sub> ) <sub>2</sub> )(P <sup>i</sup> Pr <sub>2</sub> <sup>t</sup> Bu)] (4) .....	82
4.2.5	[Co(N(SiMe <sub>3</sub> ) <sub>2</sub> )(P <sup>n</sup> Pr <sub>2</sub> OEt)] (5) .....	82
4.2.6	[Co(N <sup>t</sup> Bu(SiMe <sub>3</sub> ) <sub>2</sub> )(PMe <sub>3</sub> )] (6).....	83
4.2.7	[Co(TMP) <sub>2</sub> (PMe <sub>3</sub> )] (7) .....	83
4.2.8	[Ni(N(SiMe <sub>3</sub> ) <sub>2</sub> )(PMe <sub>3</sub> )] (8) .....	84
4.2.9	[Ni(P <sup>i</sup> Pr <sub>2</sub> <sup>t</sup> Bu) <sub>2</sub> ] (9).....	84
4.3	Deposition experiments .....	84
4.3.1	Tantalum Sulfide .....	85
4.3.2	Molybdenum Sulfide .....	86
<b>5</b>	<b>Appendix.....</b>	<b>89</b>
5.1	Crystallographic data .....	89
5.1.1	[Co(N(SiMe <sub>3</sub> ) <sub>2</sub> )(PEt <sub>3</sub> )] (3b) .....	89
5.1.2	[Co(N(SiMe <sub>3</sub> ) <sub>2</sub> )(P <sup>n</sup> Pr <sub>3</sub> )] (3c) .....	94
5.1.3	[Co(N(SiMe <sub>3</sub> ) <sub>2</sub> )(P <sup>i</sup> Pr <sub>3</sub> )] (3d).....	98
5.1.4	[Co(N(SiMe <sub>3</sub> ) <sub>2</sub> )(P <sup>n</sup> Pr <sub>2</sub> <sup>t</sup> Bu)] (4) .....	104
5.1.5	[Co(N(SiMe <sub>3</sub> ) <sub>2</sub> )(P <sup>n</sup> Pr <sub>2</sub> OEt)] (5).....	112
5.1.6	[Co(N(SiMe <sub>3</sub> <sup>t</sup> Bu) <sub>2</sub> )(PMe <sub>3</sub> )] (6).....	116
5.1.7	[Co(TMP) <sub>2</sub> (PMe <sub>3</sub> )] (7) .....	127
1.1.1	[Ni(N(SiMe <sub>3</sub> ) <sub>2</sub> )(PMe <sub>3</sub> )] (6) .....	133
5.1.8	[Ni(P <sup>i</sup> Pr <sub>2</sub> <sup>t</sup> Bu) <sub>2</sub> ] (10) .....	138
	<b>References.....</b>	<b>143</b>

# List of Figures

- Figure 1.1 Left: Trigonal planar coordination geometry of the nitrogen atom enables  $\pi$ -donation of the amido ligand p-lone pair in a vacant metal d-orbital. Right: Pyramidal coordination geometry at the nitrogen atom hinders  $\pi$ -interaction between ligand and metal orbitals.<sup>[1]</sup>..... 3
- Figure 1.2 Effect of negative axial ZFS: splitting of an  $S = 2$  state into  $M_s$  levels.<sup>[21]</sup> ..... 5
- Figure 1.3 Magnetic and relaxation behavior of a double-well potential of a double-well potential.<sup>[29]</sup>..... 6
- Figure 1.4 Left: Structure of a trigonal pyramidal amido complex [(tpaMes)Fe]. Orange, blue, and gray spheres represent Fe, N, and C atoms, respectively; H atoms have been omitted for clarity. Right: Splitting of the 3d orbital energies for a high-spin Fe<sup>II</sup> center in a trigonal pyramidal ligand field.<sup>[16]</sup>..... 8
- Figure 1.5 Left: SEM image of a substrate covered with a non-homogeneous PVD-grown film. Right: Cross-sectional SEM image of homogeneous Al<sub>2</sub>O<sub>3</sub> films deposited on Si substrate by ALD.<sup>[48]</sup>..... 10
- Figure 1.6 Schematic representation of the generation of thin films (green) on high aspect ratio substrates (grey). Left: Uniform film grown by ALD; Center: Film deposition by CVD: Inhomogeneous film growth caused by particle formation and/or shadowing effects; Right: Line of sight technology PVD: Only planar areas are covered.<sup>[49,50]</sup>..... 10
- Figure 1.7 Different growth modes of thin films (green) on a substrate (grey). Left: FRANK-VAN-DER-MERVE growth, center: STRANSKI-KRASTANOW growth, right: VOLMER-WEBER growth. <sup>[51-55,57]</sup> ..... 11
- Figure 1.8 Process schematic of a simplified CVD (left) and ALD

---

	(right) pulse sequence. Bottom: expected film growth vs. process time. <sup>[39]</sup> . . . . .	12
Figure 1.9	Schematic representation of surface reactions during an idealized 4- step ALD cycle with two precursors. Precursor 1: green-grey particles, precursor 2: orange-grey particles, byproducts: grey particles. <sup>[59]</sup> .....	13
Figure 1.10	Left: Number of adsorbed atoms depending on the precursor pulse length for CVD (dashed line) and ALD (solid line) processes. Center: Gain in film thickness within five ALD cycles. Right: Dependency of the GPC on the number of reaction cycles in different types of adsorption processes. Black line: linear film growth, orange line: substrate enhanced growth, green line: substrate-inhibited growth of type 1, grey line: substrate-inhibited growth of type 2. <sup>[59,67]</sup> . . . . .	16
Figure 1.11	Optimum deposition temperature: ALD window. <sup>[40,59]</sup> ....	17
Figure 1.12	Commonly used ligands for ALD precursors. <sup>[56,75]</sup> . . . . .	18
Figure 1.13	Periodic table overview of reported ALD processes for a) oxides, b) pure elements, c) sulfides and d) nitrides. Green boxes: Thermal ALD, grey boxes: plasma-enhanced ALD, orange boxes: both techniques reported. <sup>[66]</sup> . . . . .	20
Figure 1.14	(a) Conventional patterning consisting of film deposition, lithography, and etching. (b) Self-aligned fabrication. . . . .	22
Figure 2.1	Thermogravimetric analysis of <b>2</b> . Blue line: TG-curve, green line: DTG-curve. . . . .	30
Figure 2.2	<sup>1</sup> H NMR spectra of <b>3b</b> in C <sub>6</sub> D <sub>6</sub> . From top to bottom: pure <b>3b</b> ; compound <b>3b</b> measured after contact with air, <b>3b</b> measured after heating for 18 h at 160 °C in a stainless-steel container. . . . .	32

---

Figure 2.3	Thermogravimetric analysis of 3a-c. Solid lines: TG-curve, dotted lines: DTG-curve. ....	34
Figure 2.4	Thermogravimetric analysis of 4.....	35
Figure 2.5	Possible d-orbital splitting schemes for a trigonal planar $\text{Co}^{2+}$ complex. Left: Ideal trigonal planar geometry ( $D_{3h}$ ); center: distorted geometry ( $C_{2v}$ ); The symmetry labels ignore differences between the ligands. Right: distorted geometry ( $C_1$ ), derived from DFT calculations. <sup>[13,160,161]</sup> .....	37
Figure 2.6	Solid state structures of compound 3b-7 with the anisotropic displacement parameters drawn at 50 % probability level. The C–H hydrogen atoms are omitted for clarity. ....	38
Figure 2.7	$X_M T$ vs. $T$ plot for 3b - 5. Inset: VTVH magnetization measurements as $M_{\text{mol}}$ vs. $\mu_B B/kT$ . Solid lines represent the calculated curve fits.....	40
Figure 2.8	Frequency dependence of $\chi''$ at various temperatures with an applied dc field of $H_{\text{dc}} = 3000$ Oe for compounds 3b, 4 and 5.....	41
Figure 2.9	Correlation between axial zero field splitting parameter $D$ and N–Co–N angles (left) as well as the TOLMAN electronic parameter $TEP$ (right).....	42
Figure 2.10	UV-Vis spectra of compounds 2-5, measured in $n$ -pentane. ....	45
Figure 2.11	Left: UV-Vis spectra of compounds 1, 2, 3a, and 4 measured in $n$ -alkanes. Right: UV-Vis spectra of compounds 2, 3a, and 4 measured in THF. ....	47
Figure 2.12	VT-UV-Vis spectra of $[\text{Co}(\text{N}(\text{SiMe}_3)_2)_2(\text{PEt}_3)]$ (3b, left) and $[\text{Co}(\text{N}(\text{SiMe}_3)_2)_2(\text{P}^i\text{Pr}_2^i\text{Bu})]$ (4, right) in $n$ -hexane. ....	48

- Figure 2.13 UV-Vis spectra of 1 in *n*-hexane (left) and toluene (right) at different temperatures. .... 49
- Figure 2.14 Normalized UV-Vis spectra of 1 measured in different conc. at 80 °C in toluene..... 51
- Figure 2.15 <sup>1</sup>H NMR spectra of 4 in toluene-*d*<sub>8</sub> at different temperatures. .... 52
- Figure 2.16 Investigation of phosphine dissociation of 4 using <sup>1</sup>H NMR spectroscopy in toluene-*d*<sub>8</sub>. .... 54
- Figure 2.17 Scheme: proposed dissociation equilibrium between [Co(N(SiMe<sub>3</sub>)<sub>2</sub>)<sub>2</sub>(P<sup>*i*</sup>Pr<sub>2</sub>tBu)] (4) and [Co(N(SiMe<sub>3</sub>)<sub>2</sub>)<sub>2</sub>] (1) and P<sup>*i*</sup>Pr<sub>2</sub>tBu. Equation: Dependence of the observed chemical shift for the SiMe<sub>3</sub> groups from the ratio (x) of dissociated and not dissociated cobalt complexes 1 and 4.... 54
- Figure 2.18 Left: Curie-plot of the chemical proton shift of the SiMe<sub>3</sub> groups of 2a, derived from VT-<sup>1</sup>H NMR measurements in toluene *d*<sub>8</sub>. Right: Observed (black squares) and extrapolated chemical proton shift of the SiMe<sub>3</sub> groups of 1 (red line) and 3a (green line). .... 56
- Figure 2.19 Superimposed <sup>1</sup>H NMR spectra of [Ni(N(SiMe<sub>3</sub>)<sub>2</sub>)<sub>2</sub>(PMe<sub>3</sub>)] (8) in C<sub>6</sub>D<sub>6</sub> at room temperature directly after purification (red) and after 2 weeks of storage at room temperature (blue)..... 58
- Figure 2.20 Solid state structure of 8. .... 59
- Figure 2.21 Solid state structure of [Ni(P<sup>*i*</sup>Pr<sub>2</sub>tBu)<sub>2</sub>I] 9. .... 61
- Figure 2.22 Schematic drawing of the used ALD reactor. MFC = mass flow controller.<sup>[148]</sup>. .... 64
- Figure 2.23 XPS depth profile of a SiO<sub>2</sub> wafer treated with Ta(NMe<sub>2</sub>)<sub>5</sub> and H<sub>2</sub>S in an ALD reactor. .... 66
- Figure 2.24 XPS survey of a SiO<sub>2</sub> wafer, treated with Ta(NMe<sub>2</sub>)<sub>5</sub> and TMS<sub>2</sub>S in an ALD reactor. .... 67

Figure 2.25	Left: Two-dimensional surface profile of a SiO <sub>2</sub> wafer measured at the edge between covered and non-covered areas. Right: Topographic image of a covered SiO <sub>2</sub> wafer derived by AFM.....	69
Figure 2.26	SEM image of different samples covered by film grown by ALD. ....	70
Figure 2.27	Top: XPS spectra of two MoS <sub>2</sub> samples (red & blue graph) before (left image) and after (right image). Bottom: Deconvolution of a high-resolution XPS of a MoS <sub>2</sub> film deposited on SiO <sub>2</sub> without sputtering of the Mo 3d region. ....	71
Figure 2.28	XPS measurements of the Mo 3d region of a SiO <sub>2</sub> -wafer, covered with ALD-grown MoS <sub>2</sub> . ....	73
Figure 2.29	Left: Linear sweep cyclic voltammetry of a GC electrode covered with MoS <sub>2</sub> . ....	74
Figure 4.1	XPS survey spectrum of a SiO <sub>2</sub> wafer treated with Ta(NMe <sub>2</sub> ) <sub>5</sub> and TMS <sub>2</sub> S in an ALD reactor.....	86
Figure 5.1	Thermal ellipsoid plot of CW_JG_101016. ....	89
Figure 5.2	Thermal ellipsoid plot of CV_JEG_SS_260215. ....	94
Figure 5.3	Thermal ellipsoid plot of CW_JG_240215. ....	98
Figure 5.4	Thermal ellipsoid plot of CW_JG_051015. ....	104
Figure 5.5	Thermal ellipsoid plot of CV_JEG_011215. ....	112
Figure 5.6	Thermal ellipsoid plot of CV_JEG_210916. ....	116
Figure 5.7	Thermal ellipsoid plot of CV_031215. ....	127
Figure 5.8	Thermal ellipsoid plot of CV_JEG_031016. ....	133

# List of Schemes

Scheme 1.1 Possible reactions with Cobalt silylamido complex $[\text{Co}(\text{N}(\text{SiMe}_3)_2)_2]$ (1). <sup>[9]</sup> .....	2
Scheme 1.2 Chemical reactions for the generation of $\text{Al}_2\text{O}_3$ <i>via</i> ALD. <sup>[59]</sup> .....	14
Scheme 1.3 Simplified surface reactions during PE-ALD of $\text{TaCl}_5$ and hydrogen plasma. <sup>[40,65]</sup> .....	15
Scheme 1.4 Electrochemical water splitting with two half reactions: Hydrogen evolution reaction (HER) and oxygen evolution reaction (OER). <sup>[106]</sup> .....	24
Scheme 2.1 Synthetic protocol for the formation of cobalt silylamido phosphine complexes 3a-3d. ....	32
Scheme 2.2 Left: Proposed synthesis of $\text{HN}^t\text{Bu}_2$ . <sup>[165]</sup> Right: Tetramethylpiperidine (TMP) as alternative to $\text{HN}^t\text{Bu}_2$ .....	43
Scheme 2.3 Synthetic protocol for the formation of cobalt amido phosphine complexes 6 and 7.....	44
Scheme 2.4 Ligand dissociation, followed by monomer-dimer equilibrium between 1 and 1'. <sup>[147]</sup> .....	50
Scheme 2.5 Synthesis of $[\text{Ni}(\text{N}(\text{SiMe}_3)_2)_2(\text{PMe}_3)]$ (8). ....	57
Scheme 2.6 Proposed synthetic procedure for Ni(I) amido complexes via comproportionation. ....	63
Scheme 3.1 Synthetic overview of cobalt complexes prepared in this thesis. ....	75

## List of Tables

Table 2.1	Structural data for complexes 2-7. ....	39
Table 2.2	Magnetic data for complexes 2-5. ....	41
Table 2.3	Selected bond lengths and angles of [Ni(N(SiMe <sub>3</sub> ) <sub>2</sub> (PMe <sub>3</sub> )] ( <b>8</b> ) and literature known [Ni(N(SiMe <sub>3</sub> ) <sub>2</sub> (THF)]. <sup>[171]</sup> .....	59
Table 2.4	Selected bond lengths and angles of [Ni(P <sup>i</sup> Pr <sub>2</sub> tBu) <sub>2</sub> I] ( <b>9</b> ) and [Ni(P <sup>i</sup> Pr <sub>2</sub> ) <sub>2</sub> I]. <sup>[175]</sup> .....	61
Table 4.1	Atomic concentrations derived from XPS before and after sputtering.....	86
Table 4.2	Deposition parameters for MoS <sub>2</sub> ALD. ....	87
Table 5.1	Crystal data and structure refinement for CW_JG_101016.....	90
Table 5.2	Bond lengths [Å] and angles [°] for CW_JG_101016. ...	91
Table 5.3	Torsion angles [°] for CW_JG_101016.....	92
Table 5.4	Crystal and structure refinement data for CV_JEG_SS_260215.....	94
Table 5.5	Bond lengths [Å] and angles [°] for CV_JEG_SS_260215.....	96
Table 5.6	Torsion angles [°] for CV_JEG_SS_260215.....	97
Table 5.7	Crystal data and structure refinement for CW_ JG_240215.....	99
Table 5.8	Bond lengths [Å] and angles [°] for CW JG_240215. ..	100
Table 5.9	Torsion angles [°] for CW_JG_240215.....	102
Table 5.10	Crystal data and structure refinement for CW_JG_051015. ....	105

---

Table 5.11	Bond lengths [ $\text{\AA}$ ] and angles [ $^\circ$ ] for CW_JG_051015.....	106
Table 5.12	Torsion angles [ $^\circ$ ] for CW_JG_051015.....	109
Table 5.13	Crystal data and structure refinement for CV_JEG_011215.....	112
Table 5.14	Bond lengths [ $\text{\AA}$ ] and angles [ $^\circ$ ] for CV_JEG_011215.....	114
Table 5.15	Torsion angles [ $^\circ$ ] for CV_JEG_011215.....	115
Table 5.16	Crystal data and structure refinement for CV_JEG_210916.....	116
Table 5.17	Bond lengths [ $\text{\AA}$ ] and angles [ $^\circ$ ] for CV_JEG_210916.....	118
Table 5.18	Torsion angles [ $^\circ$ ] for CV_JEG_210916.....	124
Table 5.19	Crystal data and structure refinement for CV_JEG_031215.....	127
Table 5.20	Bond lengths [ $\text{\AA}$ ] and angles [ $^\circ$ ] for CV_JEG_031215.....	129
Table 5.21	Torsion angles [ $^\circ$ ] for CV_JEG_031215.....	132
Table 5.22	Crystal data and structure refinement for CV_JEG_031016.....	134
Table 5.23	Bond lengths [ $\text{\AA}$ ] and angles [ $^\circ$ ] for CV_JEG_031016.....	135
Table 5.24	Torsion angles [ $^\circ$ ] for CV_JEG_031016.....	136
Table 5.25	Crystal data and structure refinement for CV_JEG_030316.....	138
Table 5.26	Bond lengths [ $\text{\AA}$ ] and angles [ $^\circ$ ] for CV_JEG_030316.....	140
Table 5.27	Torsion angles [ $^\circ$ ] for CV_JEG_030316.....	141

## Abbreviations

ALD	atomic layer deposition
AFM	atomic force microscopy
C <sub>6</sub> D <sub>6</sub>	benzene-d <sub>6</sub>
CVD	chemical Vapor Deposition
EDX	energy dispersive X-ray spectroscopy
Et <sub>2</sub> O	diethyl ether
h	hour
<sup>i</sup> Pr	iso-propyl group
GPC	growth per cycle
Me	methyl
HER	hydrogen evolution reaction
HMDS	bis(trimethylsilyl)amine
<i>n</i> -BuLi	<i>n</i> -buthyllithium
NMR	nuclear magnetic resonance
Ph	phenyl
ppm	parts per million
RT	room temperature
SEM	Scanning electron microscope
<sup>t</sup> Bu	tert-Butyl group
TGA	thermogravimetric analysis
THF	tetrahydrofuran
TMS	trimethylsilyl group
TMP	2,2,6,6-tetramethylpiperidine
TMPLi	lithium 2,2,6,6-tetramethylpiperidide
XPS	X-ray photoelectron spectroscopy

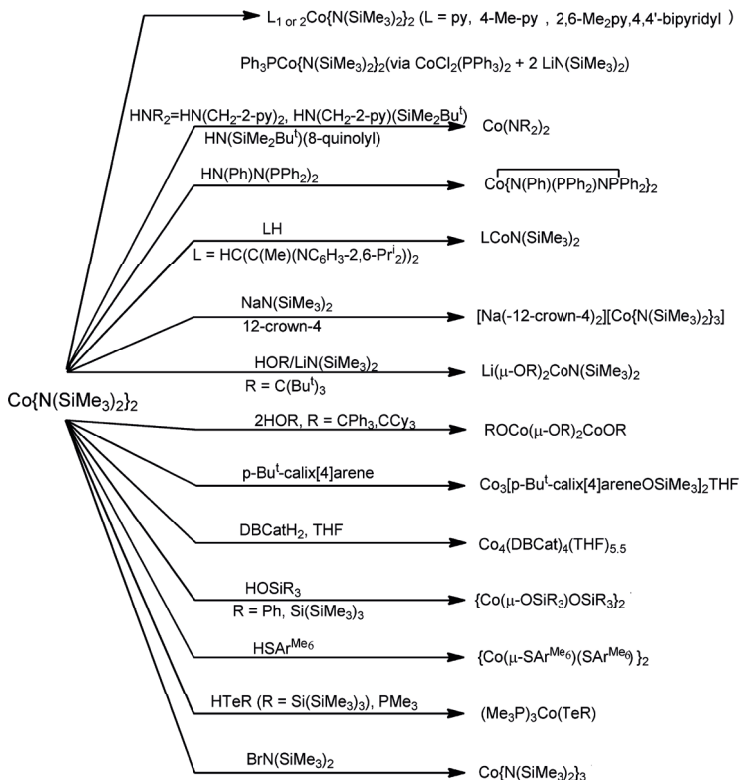
# 1 Introduction

## 1.1 The Versatile Chemistry of Low-coordinate Transition Metal Amides

Transition metal amido complexes have a tremendous span of reactivity and possible applications. Bulky amido ligands allow to stabilize open-shell transition metal complexes with unusual coordination environments and low coordination numbers. This provided the basis for the investigation of several phenomena in coordination chemistry.<sup>[1]</sup> After the first description of titanium tetrakis(diphenylamide) as one of the first transition metal amides in 1934, it took until 1959 to observe a true development in transition metal amide chemistry.<sup>[2]</sup> BRADLEY and THOMAS started a series of reports of dialkylamides of early transition metals with a rare coordination numbers between three and five ( $M(NMe_2)_n$ ,  $M = Ti^{IV}, Zr^{IV}, Nb^{IV-V}, Ta^V, Mo^{III-IV}$ , etc.).<sup>[3]</sup> It was not possible at that time to isolate amide complexes of late transition metals ions (e.g. Fe, Co, Ni), though. In 1961 BÜRGER and WANNAGAT introduced the bulky  $-N(SiMe_3)_2$  (HMDS) ligand,<sup>[4]</sup> which allowed the isolation of low coordinate metal amides of late transition metals with coordination numbers of two and three for the first time.<sup>[5,6]</sup> After the report for the preparation of two-coordinate complexes  $[Mn(N(SiMe_3)_2)_2]$ ,  $[Fe(N(SiMe_3)_2)_2]$ ,  $[Co(N(SiMe_3)_2)_2]$  and  $[Ni(N(SiMe_3)_2)_2]$ ,<sup>[5,6]</sup> focus of transition metal chemistry turned to the examination of three-coordinate amido complexes, including the report of several lanthanide containing compounds.<sup>[7,8]</sup> The group of POWER has heavily investigated strictly two-coordinated transition metal complexes since the 1980's, including the publication of solid state structures of two-coordinated iron amido complexes.<sup>[8]</sup>

Many metal amido complexes are highly reactive. This is expressed by their exceptional sensitivity towards moisture and oxygen. Mostly sterically demanding alkyl- and silylamides are used as ligands in order to provide steric shielding. This makes metal amido complexes highly soluble in aprotic hydrocarbon solvents, rendering this compound class a versatile source for hydrocarbon soluble metal ions. Insertion reactions into the M–N bond or M–N bond cleavage reactions with protic molecules are mostly observed. The reactivity of amido complexes was also used to activate small molecules like  $N_2$  or CO.<sup>[9]</sup> In 1995, CUMMINS and coworkers reported a planar three-coordinate  $Mo^{III}$  complex with bulky amido ligands, which was able to activate  $N_2$ .<sup>[10]</sup>

Since then, multidentate amido ligands like pincer ligands and podants have been used to investigate and tune the reactivity of transition metal complexes.<sup>[11]</sup> The rich coordination chemistry of metal amides is exemplified in Scheme 1.1, where possible reactions of the low-coordinate cobalt complex  $[\text{Co}(\text{N}(\text{SiMe}_3)_2)_2]$  (**1**) are presented.



Scheme 1.1 Possible reactions with Cobalt silylamido complex  $[\text{Co}(\text{N}(\text{SiMe}_3)_2)_2]$  (**1**).<sup>[9]</sup> Adapted with permission from ref. 9. Copyright 2012 American Chemical Society.

In the solid state, the nonpolar coordination environment causes high volatility. Many transition silylamides can be sublimed at temperatures below 100 °C at 0.01 mbar. For this reason, metal amides are used as precursors in several depositions techniques like atomic layer deposition.<sup>[1,12]</sup> In transition metal complexes coordinated by two bulky silyl amides, most of the spin-orbit coupling remains

unquenched, resulting a high magnetic anisotropy and other interesting magnetic properties of these compounds. The coordination geometry also has a high impact on their magnetic properties.<sup>[9,13–15]</sup> Therefore, the magnetic properties of low coordinate transition metal amido complexes returned into the scientific focus, when single molecular magnetism was reported (see Section 1.2.2).<sup>[16,17]</sup>

In the following chapters, fundamental concepts and possible applications for transition metal amide complexes will be presented. First, fundamental concepts of metal amides like their coordination chemistry and their magnetic properties will be highlighted. In the second section, focus will be on the application of transition metal compounds deposition techniques and electrocatalysis.

## Bonding Situation in Transition Metal Amido Complexes

Amido ligands are considered as both strong  $\sigma$ - and  $\pi$ -donors. The coordination geometry at the nitrogen atom can either be pyramidal or trigonal planar. In the first case,  $\pi$ -overlap between the nitrogen lone pair and valence orbitals of the metal center is hindered (see Figure 1.1, right). Most transition metal amide complexes show a planar coordination geometry at the nitrogen atom, pointing towards  $sp^2$ -hybridization. In this case,  $\pi$ -bonding is achieved via the interaction of the p-orbital lone pair of the nitrogen atom and vacant valence d-orbitals at the metal center (see Figure 1.1, left). It should be noted that the inversion barrier for pyramidal coordinated nitrogen ligands is usually low, which may let them appear in a quasi-planar coordination sphere. Distinguishing the electronic situation of the nitrogen atom on the basis of its coordination chemistry can therefore lead to misjudgments<sup>[1]</sup>

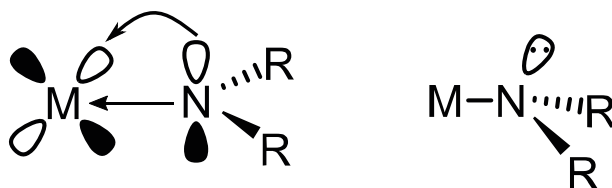


Figure 1.1 Left: Trigonal planar coordination geometry of the nitrogen atom enables  $\pi$ -donation of the amido ligand p-lone pair in a vacant metal d-orbital. Right: Pyramidal coordination geometry at the nitrogen atom hinders  $\pi$ -interaction between ligand and metal orbitals.<sup>[1]</sup>

As mentioned above, only alkylamido complexes of early transition metals could be isolated. When using silylamides, isolation of silylamido complexes of late transition metals is possible, though. Many attempts to rationalize these observations have been made.<sup>[1]</sup> One addresses the mismatch of “soft” metal centers and “hard” amido ligands.<sup>[18]</sup> In another attempt it was assumed, that the strong  $\sigma$ - and  $\pi$ -donor abilities of amido ligands lead to electronic repulsion with a late transition metal centers where the valence orbitals are already occupied, preventing the formation of late transition metal alkylamido complexes.<sup>[3]</sup> However, BERCAW and coworkers showed that the bond energy between metal centers and amido ligands not weaker as it is expected from their corresponding nitrogen–hydrogen bonding dissociation energies.<sup>[19]</sup> The distinction between the stability of alkyl- and silylamido transition metal complexes can be rationalized by hyperconjugation involving silicon and nitrogen orbitals. This so-called  $\alpha$ -silicon effect stabilizes the negative charge of the amido ligand.<sup>[20]</sup> Silylamides are also considered to be weak  $\pi$ -acceptors, due to the mixing with vacant  $\pi$ -antibonding  $\text{NSi}_2$  orbitals.<sup>[1]</sup>

## 1.2 Molecular Magnetism of Low-Valent Transition Metal Compounds

The stabilization of low coordination numbers with sterically demanding amido ligands allow to investigate unusual coordination environments, like linear or trigonal-planar coordination. These low coordination numbers go mostly in hand with interesting electronic and magnetic properties of the coordinated metal center.<sup>[9]</sup> Recently, the magnetic properties of low-coordinate transition metal complexes gained much attention.<sup>[17,21–24]</sup> Linear coordination of transition metal complexes can lead to a high degree of magnetic anisotropy, rendering these molecules a so-called single molecule magnet (*vide infra*). To understand the correlation between the coordination geometry of transition metal complexes and their magnetic properties, a brief introduction into the field of molecular magnetism will follow.

### 1.2.1 Origins of Molecular Magnetism

The finding of a hysteresis in the magnetization of a single molecule opened a new field of research, dealing with so-called single ion or single molecule magnets (SIM / SMM). The rise of molecular magnetism can be traced back to the report of a polynuclear  $\text{Mn}_{12}$  cluster in 1993 which exhibits magnetic hysteresis at low temperatures.<sup>[25]</sup>

Magnetic hysteresis is observable when a molecule shows magnetic anisotropy, which describes the preferred orientation of a spin in a system.<sup>[22]</sup> As a result of magnetic anisotropy, the system exhibits a barrier for the re-orientation of its magnetization. When a molecule's spin is  $S > \frac{1}{2}$  and the symmetry is low (which is the case in low coordinate amido complexes) a separation of excited states may occur, which then mix through spin-orbit coupling.<sup>[21,26]</sup> This phenomenon is called zero-field splitting (ZFS) and can be expressed via the following Hamiltonian:

$$\hat{H} = D \left( \hat{S}_z^2 - \frac{S(S+1)}{3} \right) + E(\hat{S}_x^2 - \hat{S}_y^2)$$

$D$  is defined as the axial and  $E$  as the rhombic ZFS parameter, while  $\hat{S}$  describes the spin projection along a given axis. Spin-orbit coupling (SOC) is distinguished in first order spin-orbit coupling (in-state spin-orbit coupling) and second order spin-orbit coupling (out-of-state spin-orbit coupling).<sup>[27]</sup> First order SOC is caused by the direct mixing of spin and angular momentum in the electronic ground state of a system, while second order SOC arises from mixing of the ground state (with no first order SOC) with excited states which possess first order SOC.<sup>[17,26]</sup> As illustrated in Figure 1.2, negative axial ZFS leads to the splitting of an  $S = 2$  state into its constituent  $M_s$  levels. Simply speaking, ZFS is based on lifting the degeneracy of  $2S+1$  microstates into magnetic spin states  $\pm M_s$  in the absence of an external magnetic field. The magnitude that arises from ZFS, is given by the spin-orbit coupling parameter  $\lambda$  which is inverse proportional to the spin  $S$ <sup>[17,21]</sup>.

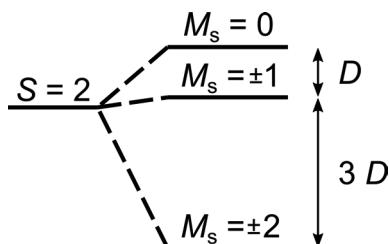


Figure 1.2 Effect of negative axial ZFS: splitting of an  $S = 2$  state into  $M_s$  levels.<sup>[21]</sup>

As introduced before, the foundation of molecular magnetism is the occurrence of magnetic hysteresis of a spin system. So far, magnetic hysteresis is only observable at very low temperatures. The highest reported temperature at